Front. Earth Sci. 2020, 14(2): 446–461
https://doi.org/10.1007/s11707-019-0786-4

RESEARCH ARTICLE

Spatial pattern analysis of post-fire damages in the Menderes District of Turkey

Emre ÇOLAK (✉), Filiz SUNAR

Civil Engineering Faculty, Istanbul Technical University, Istanbul 80626, Turkey

Abstract Forest fires, whether caused naturally or by human activity can have disastrous effects on the environment. Turkey, located in the Mediterranean climate zone, experiences hundreds of forest fires every year. Over the past two decades, these fires have destroyed approximately 308000 ha of forest area, threatening the sustainability of its ecosystem. This study analyzes the forest fire that occurred in the Menderes region of Izmir on July 1, 2017, by using pre- and post-fire Sentinel 2 (10 m and 20 m) and Landsat 8 (30 m) satellite images, MODIS and VIIRS fire radiative power (*FRP*) data (1000 m and 375 m, respectively), and reference data obtained from a field study. Hence, image processing techniques integrated with the Geographic Information System (GIS) database were applied to a satellite image data set to monitor, analyze, and map the effects of the forest fire. The results show that the land surface temperature (*LST*) of the burned forest area increased from 1 to 11°C. A high correlation (R = 0.81) between *LST* and burn severity was also determined. The burned areas were calculated using two different classification methods, and their accuracy was compared with the reference data. According to the accuracy assessment, the Sentinel (10 m) image classification gave the best result (96.43% for Maximum Likelihood, and 99.56% for Support Vector Machine). The relationship between topographical/forest parameters, burn severity and disturbance index was evaluated for spatial pattern distribution. According to the results, the areas having canopy closure between 71%–100% and slope above 35% had the highest burn incidence. As a final step, a spatial correlation analysis was performed to evaluate the effectiveness of MODIS and VIIRS FRP data in the post-fire analysis. A high correlation was found between FRP-slope, and FRP-burn severity (0.96 and 0.88, respectively).

Received April 8, 2019; accepted August 14, 2019

E-mail: colakem@itu.edu.tr

Keywords remote sensing, GIS, spectral indices, disturbance index, land surface temperature, burn severity

1 Introduction

Forests are an important natural resource that preserve the environmental balance. It has been observed across the globe that the health of a forest is a true indication of the current ecological conditions (Jaiswal et al., 2002). In recent years, forest health has been threatened due to natural disturbances caused by climate change. Despite various forest disturbances, that affect the balance of the ecosystem, e.g., insect outbreaks, disease, frosts, and windthrow, forest fires are the most destructive (Gonçalves and Sousa, 2017; Seidl et al., 2017). A forest fire is a natural phenomenon that inherently affects the environment, economy, and the well-being of society (Chowdhury and Hassan, 2015; Chaparro et al., 2016). Environmentally, forest fires affect vegetation composition and structure, as well as biogeochemical cycles such as the carbon cycle of burned areas (Flannigan et al., 2000). The frequent occurrence of a fire depends on numerous physical, chemical, and biological relations. Hence, the occurrence of fires due to natural causes can vary from one location to another depending on vegetation, weather, climate, and topography (Akkaş et al., 2006).

Parameters such as frequency, size, intensity, severity, type, and seasonality can also affect a fire. Fire frequency is the life cycle of a fire within a defined area and time period, and varies regionally as a function of a natural or human induced fire. Fire intensity is equivalent to the quantity of released energy during the fire, and can greatly differ dependent on topography, meteorological impacts, fuel type, etc. Fire severity is the measurement of the fuel consumption and the depth of the burn in surface layers. This is important for the post-fire ecosystem structure adjustment. Fire type classifies fires as crown, surface, or

ground fires. Seasonality provides significant information on the ecological evolution and relationship between fire and vegetation within the fire regime. Additionally, forest fires are highly related to weather and climate. Not only does climate and weather affect forest fires, but a fire can also affect climate or weather. Large forest fires change the albedo and vegetation structure in the region and affect the climate and energy budget (Flannigan et al., 2000; Peterson and Liittell, 2013; Platt et al., 2015).

Fires are prevalent in many forest ecosystems across the globe and are one of the fundamental factors that affect Mediterranean-type ecosystems. Located in the Mediterranean region, Turkey has a high rate of forest fires, mainly due to weather conditions. In addition to the high temperatures, the relative humidity and wind speed in the Mediterranean and Aegean regions of Turkey are also important parameters that can increase the risk of fire (Akkaş et al., 2006). According to Turkey's General Directorate of Forestry, 2411 forest fires occurred in 2017, more than 90% of which were caused by human activity. The total damage was recorded at 11993 ha, with 75% occurring in productive high forests that contribute to biodiversity. Man-made fires are generally classified as either intentional (e.g., terror attacks or incursion) or unintentional (e.g., hunting or picnics) (Sunar and Özkan 2001). Additionally, some productive forestland is allocated to mining companies, thus increasing the threat from mining activities (Gençay and Birben, 2018).

Given today's developments with remote sensing, integrated with Geographical Information System (GIS), a cost-effective and time-efficient solution for fire damage analysis can be achieved by determining fire intensity, severity, and the extent of burned area. The most widely used method to analyze the short- and/or long-term effects of fire and to determine the severity of the burn includes spectral burn indices (such as Normalized Burn Ratio (NBR)) which separates the burned area from other surface features (such as water, dark soil, etc.). The land surface temperature (LST) determined from the image data is also a significant parameter for evaluating the post-fire alteration of the environment (Vlassova et al., 2014). Fire radiative power (FRP), which is fire energy measured in megawatts per unit of time (Vadrevu and Lasko, 2018), is also used to determine approximate fire intensity. FRP is sensitive to variations in biomass density. The correlation between fire occurrence, topography, and meteorological parameters can be assessed by a spatial pattern analysis using GIS and remotely sensed data (Diaz-Delgado et al., 2004). Hence, the integration of remotely sensed data with GIS, specifically designed for applying broad-scaled tasks for geographical purposes, is crucial for revealing spatial relationships and achieving complete results, which can enhance the comprehension of forest fires (Sonti, 2015; Valero et al., 2018). As shown in many studies, this integration provides an efficient and cost-effective tool for not only estimating where and when forest fires will likely take place, but also for monitoring and mapping forest fires at local, regional, and global scales (Chuvieco and Congalton, 1989; Sonti, 2015; Flannigan et al., 2000).

This application-oriented research paper aims to evaluate the forest fire that occurred in the Menderes District of Izmir using pre- and post-fire satellite image maps and ancillary data (i.e., field data, forest management plans produced by Izmir Forest Directorate, meteorological data) in GIS. Moreover, the integration of MODIS and VIIRS FRP data with EO data and auxiliary data in GIS has not been studied extensively; therefore, this study also investigates the effectiveness of MODIS and VIIRS FRP data for post-fire analysis in GIS, i.e., its spatial correlation with burn severity and slope.

2 Study area and data used

The Menderes District, is located within the border of the Izmir Forestry Chief Directorate in the Aegean section of Turkey (Fig. 1). The forest fire in this study started in a maquis shrubland on July 1, 2017 and continued for four days.

Studies show that fires in Turkey typically occur in Black Pine (*Pinus nigra Arnold*) and Calabrian Pine (Turkish pine or *Pinus brutia Ten.*) forests due to their extreme burnability. According to the forest management plans created by the Izmir Forestry Chief Directorate, the Menderes District is mostly covered with the Calabrian pine (*Pinus brutia*) tree species with a variance in elevation between 100 m and 450 m (Fig. 1(b) and (c)). Due to the high canopy closure (71%–100%), resulting in natural branch pruning, debris, and a large number of dead plants, the risk of fire spread is greatly increased. Moreover, previous forest fires indicate that slope within the range of 8 to 35% may cause broad forest fires (Akkaş et al., 2006). In the study area, the slope is between 2° and 68°.

Meteorological data (mean and maximum wind velocity, wind direction, mean relative humidity (%), mean air temperature (°C), mean atmospheric pressure) were acquired from the Menderes meteorological station (Fig. 1(a)) close to the fire region. Before the fire, the average weather temperature in June 2017 was 25.6°C and the mean relative humidity was 42.1%. However, at the time of the fire, the average temperature of the region was 35°C and the maximum temperature reached to 42°C (Fig. 2). During the fire, the wind direction was from the north and northeast and the average wind speed measured at 7 m/s. The average relative humidity was 30%.

Wind speeds between 3 and 9 m/s have caused large forest fires in Turkey (Akkaş et al., 2006). Table 1 shows that the high air temperature and wind speed in the region affected the forest fire in the Menderes District.

For this study, the following data sources were utilized:

- Landsat 8 satellite images acquired before (June 30, 2017) and after (July 16, 2017 and November 1, 2018) the

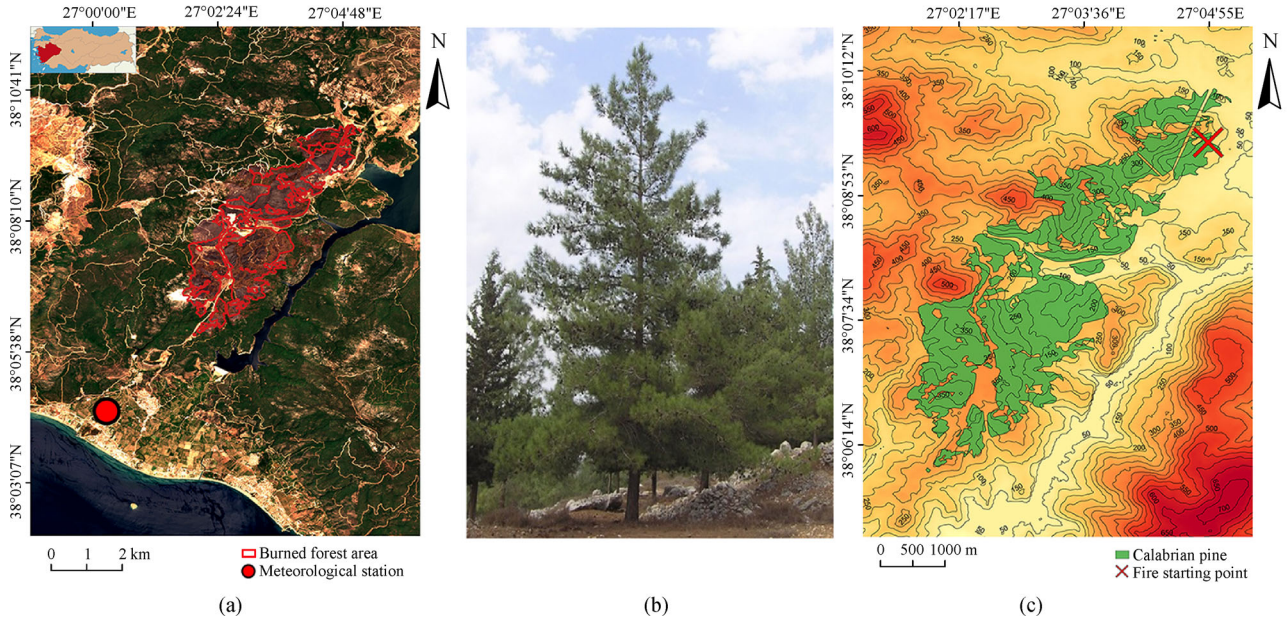

Fig. 1 Study area. (a) Satellite image, (b) tree species- Calabrian Pine (*Pinus brutia*), (c) elevation map.

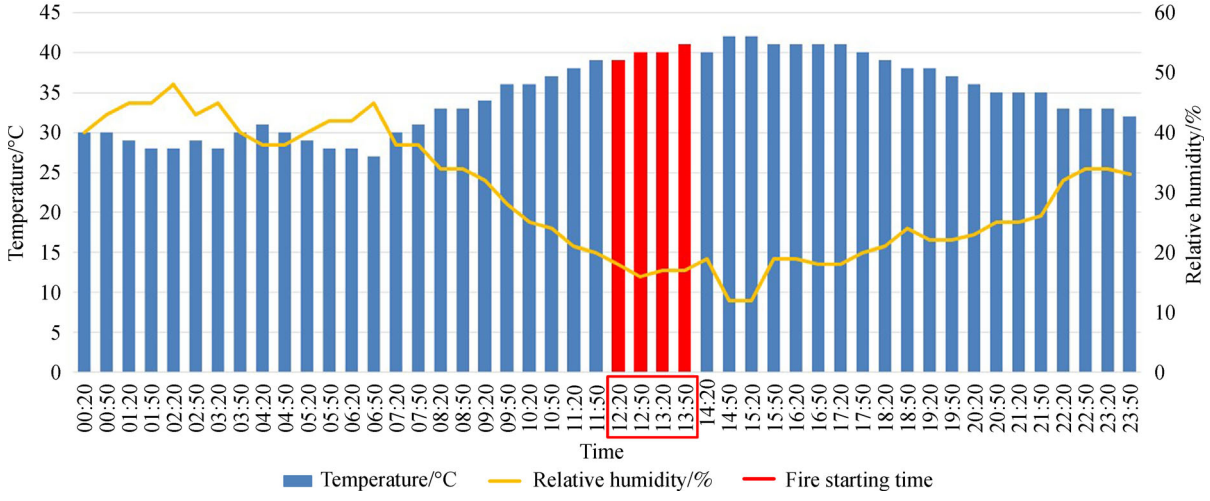

Fig. 2 Air temperature and relative humidity of the Menderes District on July 1, 2017 (Meteorological Service 2018).

Table 1 Meteorological parameters affecting a forest fire in Turkey (Akkaş et al., 2006)

Parameters	Optimum values	Average values in the Menderes District
Temperature	> 25°C	35°C
Wind speed	3–8.8 m/s	7 m/s
Relative humidity	< 40%	30%

forest fire (downloaded from USGS Website).

- Sentinel-2A satellite images acquired after (July 22, 2017) the forest fire (downloaded from Copernicus Website).
- GIS data created by using existing forest maps and forestry management plans along with the field study conducted by Izmir Forestry Chief Directorate after the forest fire.
- MODIS and VIIRS FRP data acquired during the fire (July 1, 2017) (downloaded from NASA Webstie).

As a moderate-resolution satellite (from 15 m to 100 m), Landsat 8 consists of 11 spectral bands and operates in the visible/near-infrared, shortwave infrared, and thermal infrared spectrums. In comparison, the Sentinel-2 satellite has 13 spectral bands at different spatial resolutions ranging from 10 m to 60 m in the visible/near-infrared and shortwave infrared spectral range. Moreover, the MODIS instrument consists of 36 spectral bands ranging in wavelengths from 0.4 μm to 14.4 μm in three different

spatial resolutions, i.e., 250, 500, and 1000 m. MODIS FRP used in this study has a 1000 m spatial resolution (Giglio et al., 2018). The VIIRS instrument has 22 bands ranging from 0.412 μm to 12.01 μm wavelengths in two different spatial resolutions, i.e., 375 and 750 m. The active fire data set used in this study has a 375 m spatial resolution; however, the FRP was obtained utilizing the co-located dual-gain mid-IR M13 channel (750 m) for all fire pixels detected using 375 m data and then divided by two to retrieve 375 m FRP (Vadrevu and Lasko, 2018). Since the VIIRS FRP and the MODIS FRP are retrieved using the 4.0 μm channel, and both cross the equator at approximately the same time (1:30 a.m. descending and 1:30 p.m. ascending) locally, FRP data sets have a strong correlation. According to Vadrevu and Lasko (2018), the correlation coefficient between VIIRS FRP and MODIS FRP was found as $R = 0.99$.

3 Methodology

In this study, various image-processing steps, such as spectral burn indices, determination of burn severity, *LST* determination, image classification, correlation analysis, and GIS data integration were applied to evaluate forest fire effects both quantitatively and qualitatively.

As summarized in Fig. 3, the first step was to acquire the Sentinel 2A and Landsat 8 satellite images. The second pre-processing step involved radiometric and geometric corrections. For the radiometric correction, the histogram matching operation was performed between Landsat 8 and Sentinel 2 satellite images. For the geometric correction, Landsat 8 images were used as a base image and Sentinel 2 images were registered to Landsat images using a rectification process. For this purpose, 25 Ground Control Points (GCPs) were selected and marked on Sentinel 2 images. The 10 m and 20 m spatial resolution Sentinel 2 satellites images were georeferenced with ±0.257 and ±0.258 rms (Root Mean Square) error, respectively. The study area was then subsetted from all the image data sets used. Additional processing steps are outlined in the following sections.

3.1 Fire risk mapping

A forest fire risk map depends on various environmental and topographical parameters, such as slope, aspect, canopy closure, and vegetation species. Sivrikaya et al. (2014) outlined the main fire risk variables for the Turkish forests in Table 2. The relative weights for variables were determined objectively based on the literature (Jaiswal et al., 2002; Sivrikaya et al., 2014) and historical data analysis.

In Table 2, the fire risk ratings (i.e., low, moderate-low, moderate-high, and high) were assigned to main variables. To this end, classes with relatively higher historical fire incidence were given higher rates than those in other classes. Research shows that topography is the most significant parameter for fire behavior, as fire spreads faster when slope increases. In addition to being covered with Black pine and Calabrian pine species, Turkish forests are at high risk due to a canopy closure of more than 71%. Aspect is also an important variable for evaluating the risk of fire. The south-facing sections of Turkish forests are considered to be more sensitive to fire than other areas (Sivrikaya et al., 2014; Akkaş et al., 2006). Based on these

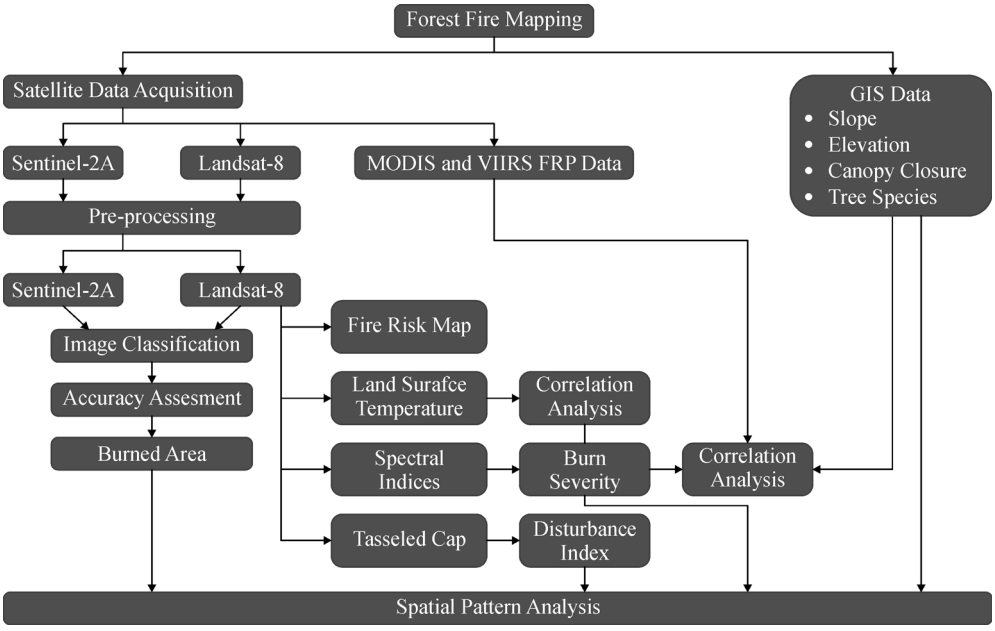

Fig. 3 Flow chart of the study.

variables, the fire risk map of the Menderes District was produced by overlaying all the input layers according to their weights (Table 2).

3.2 Spectral indices

The brightness values of multiple bands can be used in mathematical operations, which hence reveal and isolate information about target features. In this context, spectral vegetation and/or spectral burn indices are used for the immediate assessment of the canopy biomass after a forest fire. Several spectral indices used in this study are given in the Table 3.

The *NDVI* is the most popular vegetation index, as it provides a measure of vegetation greenness and photosynthetic activity (Fraser et al., 2000). The *BAI* is primarily utilized for the detection and enhancement of the burned (char) signal. The *BAI* computes the spectral distance from each pixel to the combination of burned pixels as a reference point in red near infrared (*R-NIR*) bi-spectral space. The *NBR* is specifically designed to extract the burned areas and determine burn severity. It uses the Near Infrared (*NIR*) and Shortwave Infrared (SWIR) bands, which are different from the *NDVI* (i.e., Red and *NIR* bands) calculation. In general, healthy vegetation has a high *NIR* reflectance and low SWIR reflectance in the EM spectrum. However, burned areas have low reflectance in *NIR* and high reflectance in SWIR bands. Unlike NBR, *NBRT* is normalized with a thermal band to enhance post-fire changes (Holden et al., 2005; Key and Benson, 2005; Schepers et al., 2014; Giannini et al., 2015).

Table 2 Fire risk variables and classes (Sivrikaya et al., 2014)

Variables	Classes	Fire risk ratings
Slope (weight = 5)	0%–5%	Low
	5%–15%	Moderate-Low
	15%–35%	Moderate-High
	> 35%	High
Vegetation Species (weight = 10)	Oak and Coppice	Low
	Degraded areas	Moderate-Low
	Beech and Fir	Moderate-High
	Black pine and Calabrian pine	High
Canopy Closure (weight = 5)	< 11%	Low
	11%–40%	Moderate-Low
	41%–70%	Moderate-High
	71% >	High
Aspect (weight = 3)	0–23 N	Low
	23–68 NE	Moderate-Low
	68–113 E	Moderate-Low
	113–158 SE	Moderate-High
	158–203 S	High
	203–248 SW	High
	248–293 W	Moderate-High
	293–338 NW	Moderate-High
	338–360 N	Low

3.3 Burn severity

Burn severity calculates the magnitude of ecological alteration caused by a forest fire. *NBR* is also crucial for determining, measuring, and mapping burn severity quantitatively and qualitatively (Key and Benson 2005). Hence, as shown in Eq. (1), the post-fire *NBR* data set is subtracted from the pre-fire *NBR* data set to generate a scaled index (d*NBR*) of the burn severity. This index (d*NBR*) is compatible with land measurements observed in the Mediterranean forest areas (Norton, 2008).

$$\mathrm{d}NBR = NBR_{\mathrm{pre-fire}} - NBR_{\mathrm{post-fire}} \quad (1)$$

NBR index values theoretically vary from -1 to $+1$, whereas d*NBR* values can vary from -2 to $+2$. In general, the burn severity category indicated by the US Geological

Table 3 Spectral Indices used in this study

Spectral index	Formulation	References
Normalized Difference Vegetation Index (*NDVI*)	$NDVI = \frac{(NIR - \mathrm{R})}{(NIR + \mathrm{R})}$	Tucker, 1979
Burn Area Index (*BAI*)	$BAI = \frac{1}{(0.1 - \mathrm{Red})^2 + (0.06 - NIR)^2}$	Schepers et al., 2014
Normalized Burn Ratio (*NBR*)	$NBR = \frac{(NIR - SWIR)}{(NIR + SWIR)}$	Key and Benson, 2005
Normalized Burn Ratio-Thermal (*NBRT*)	$NBRT = \frac{\left(NIR - SWIR\left(\frac{TIR}{1000}\right)\right)}{\left(NIR + SWIR\left(\frac{TIR}{1000}\right)\right)}$	Holden et al., 2005

Survey (USGS) is used as a reference in the burn severity evaluation (Table 4).

Table 4 d*NBR* severity category definitions (©USGS)

dNBR	Burn severity
< -0.25	High post-fire regrowth
-0.25 to -0.1	Low post-fire regrowth
-0.1 to $+0.1$	Unburned
0.1 to 0.27	Low-severity
0.27 to 0.44	Moderate-low severity
0.44 to 0.66	Moderate-high severity
> 0.66	High-severity

3.4 Land surface temperature determination

Thermal infrared (TIR) images, based on the principle that all objects with a temperature above absolute zero emit energy, are used to determine *LST*. Many algorithms have been developed to determine *LST*, such as mono-window, split-window, single channel, temperature-emissivity separation, and the land surface temperature algorithm. The land surface temperature algorithm, customized for Landsat 8 for computing *LST*, involves the following main stages (Table 5): i) transformation of digital numbers (DN) to spectral radiance values; ii) transformation of spectral radiance values to brightness temperature values; iii) computing the surface emissivity (ε) values; and iv) calculating the land surface temperature (Yu et al., 2014; Dağlıyar et al., 2015; Giannini et al., 2015; US Geological Service, 2016). In this study, thermal bands 10 and 11 of TIRS sensor of Landsat 8, which have 100 m spatial resolution, were used to determine the land surface temperature.

As seen in Table 5, *NDVI* was used to calculate the surface emissivity (ε) values. Since the pixel values of the study area are a mixture of vegetation and bare soil ($0.2 \leqslant NDVI \leqslant 0.5$), P_v was calculated by using *NDVI* values. Surface emissivity (ε), an important parameter for calculating the temperature of bodies, is defined as the ratio of the incoming energy beam to the absorbed energy beam. The emissivity values of the objects depend on the wavelength of the emitted radiation and the geometric position of the objects (Dağlıyar et al., 2015). In the land surface temperature algorithm, *LST* accuracy primarily depends on emissivity. The algorithm is confirmed to retrieve emissivity using *NDVI* values since the it is tested by in situ measurements. As a result, root mean square error ($\pm$rmse) has been shown to be less than ± 0.005 over vegetative areas (Jimenez-Munoz et al., 2009).

To determine the land surface temperature difference (d*LST*), the following formulation was used.

$$\mathrm{d}LST = LST_i - LST_j \tag{2}$$

Table 5 The stages of LST calculation

Stage	Formulation	Explanation
i	$L_\lambda = M_L \times Q_{cal} + A_L$	L_λ = spectral radiance (W/(m^2 × sr × μm)) M_L = band-specific multiplicative rescaling factor from the metadata A_L = band-specific additive rescaling factor from the metadata Q_{cal} = L1 pixel value as digital number
ii	$T = \dfrac{K2}{\ln\left(\dfrac{K1}{L_\lambda} + 1\right)}$	T = brightness temperature (K) $K1$ = band-specific thermal conversion constant from the metadata $K2$ = band-specific thermal conversion constant from the metadata
iii	$NDVI = \dfrac{NIR - Red}{NIR + Red}$	$NDVI = \begin{cases} NDVI < 0.2, \varepsilon = 0.97; \\ NDVI > 0.5, \varepsilon = 0.99; \\ 0.2 \leqslant NDVI \leqslant 0.5, \varepsilon = \varepsilon_v \times P_v + \varepsilon_s \times (1 - P_v) + d\varepsilon; \end{cases}$ ε_v: vegetation emissivity; ε_s: soil emissivity; P_v: proportion of vegetation; $d\varepsilon$: comprise the impact of geometrical distribution of the natural surfaces and also the internal reflections: $d\varepsilon = (1 - \varepsilon_s) \times (1 - P_v) \times F \times \varepsilon_v$, F: geometrical factor ranging from 0 to 1, contingent on the geometrical distribution of the surface, that is typical 0.55 $Pv = \left(\dfrac{NDVI - NDVI_{min}}{NDVI_{max} + NDVI_{min}}\right)^2$
iv	$LST = \dfrac{T}{1 + \left(\dfrac{\lambda \times T}{\rho}\right) \times \ln(\varepsilon)}$	λ = the central band wavelength of emitted energy $\rho = h \times c/\sigma$ (1.438×10^{-2} m × K) h = the Planck constant (6.626×10^{-34} J×s) c = speed of light (2.99792×10^8 m/s) σ = the Boltzmann constant (1.38×10^{-23} J/K)

where LST_i is the July 16, 2017 dated post-fire image, and LST_j is the June 30, 2017 dated pre-fire image.

3.5 Correlation analysis

Previous forest fire studies have shown a relationship between *LST* differences and burn severity. In this context, high *LST* corresponds to high burn severity and low *LST* corresponds to low burn severity (Holden et al., 2005). Moreover, the spatial distribution of *LST* in burned areas depends on burn severity (Vlassova et al., 2014). In this study, a correlation analysis was performed between d*LST* and d*NBR* index values obtained from the pre- and post-fire Landsat 8 satellite images of the Menderes District. Furthermore, to reveal the potential correlations of other spectral burn indices (*BAI* and *NBRT*) with d*LST*, the differences of pre- and post-fire Landsat 8 images (d*BAI* and d*NBRT*) were obtained and a correlation analysis was performed.

Higher intensity fires lead to significant environmental changes post-fire; thus the correlation with burn severity (Boschetti and Roy, 2009; Heward et al., 2013). Many studies support that *FRP*, as the energy radiated by the fire per unit of time, could be described as a remote measure of fire intensity. Hence, *FRP* data acquired from VIIRS during the fire was also used in the correlation analysis. Furthermore, *FRP* is inherently related to topography, and especially to slope (Valero et al., 2018).

3.6 Image classification

In this study, a supervised classification approach, most commonly used for the quantitative analysis of remote sensing image data, is applied. It is described as a thematic mapping of the landscape labels that represent the land cover types of interest using the measurement space of the sensor (Richards, 2013). As classifiers, Maximum Likelihood (ML) and Support Vector Machines (SVM) are used.

In the Maximum Likelihood classification, a pixel is assigned to the class that has the highest probability value, assuming that each class of training data has a Normal (Gaussian) distribution. A probability distribution model is needed to calculate these probabilities. Support Vector Machines are an efficient statistical classification method that determines how to define the boundary line (hyperplane) that can best distinguish two or more classes from each other. The way the boundary line is defined depends on the training data used for the classification and the characteristics of the classes to be considered. For the SVM classification, a nonlinear boundary was used, and in general, the free parameters of SVM (C: trades off misclassification of training samples against the simplicity of the classification boundaries, and γ: defines how far the influence of a single training sample reaches) was tuned using a grid search in this study.

The performance of the two classification methods used was evaluated using independent test pixels. In this context, 75 samples were used for each class as a training data set. Apart from the data set used for training, 50 samples were randomly selected for each class as a test data set.

3.7 Distribution index

The Disturbance Index (*DI*) based on the Tasseled Cap transformation is an efficient way to detect the forest vegetation disturbance. The *DI* is a linear combination of the Tasseled Cap indices (which are Brightness (B), Greenness (G), and Wetness (W)) and can be calculated by using Normalized Tasseled Cap Indices (Table 6) (Chen et al., 2012). The *DI* transformation is based on the observation that disturbed stands typically have a higher brightness value and lower wetness and greenness values when compared to undisturbed forest area.

3.8 GIS integration

In this stage, integrated remote sensing and GIS analysis were employed to examine the main spatial patterns of the forest fire in Menderes. Spatial relationships and layer overlay techniques were used to analyze the interactions between fire disturbances and topographical/forest parameters. Sentinel-2A and Landsat 8 post-fire processed data was integrated with GIS data for this purpose.

4 Results and discussion

As seen from the fire risk map, (Fig. 4(a)), the areas

Table 6 DI calculation

Explanation	Formulation
Determination of normalized tasseled cap indices	$B_n = (B - B_\mu)/B_\sigma$ $G_n = (G - G_\mu)/G_\sigma$ $W_n = (W - W_\mu)/W_\sigma$ B_μ, G_μ, and W_μ: mean Tasseled Cap Brightness, Greenness and Wetness B_σ, G_σ, and W_σ: corresponding standard deviations R_n, G_n and W_n: normalized Brightness, Greenness and Wetness
Calculation of DI	$DI = B_n - (G_n + W_n)$

affected by the fire were primarily found to be moderate-high risk (Table 7). In the spectral indices analysis, *NBR* index was found to be the most efficient index for extracting burned areas (Fig. 4(b)). Nonetheless, when compared to the *NDVI* image (Fig. 4(c)), both were found to be very efficient for immediate assessment.

To generate the burn severity (d*NBR*), the *NBR* data set of post-fire dated July 16, 2017 was subtracted from the pre-fire *NBR* data set dated June 30, 2017 (Fig. 5(a)). To monitor vegetation survival and mortality of burned areas with (moderate-high)/high burn severity in a short-term, *NDVI* was applied to the most recent cloudless image after the fire, i.e., Landsat 8 satellite image dated November 1, 2018 (Fig. 5(b)). As seen from the *NDVI* map (Fig. 5(b)), there is no evidence that the vegetation in the area grew back after 15 months. In fact, the latest satellite image taken from Google Earth shows that this was due to the start of the mining operations in the northern part of the region, proving its negative impacts on forest regeneration (Fig. 5(c)).

As expected, the land surface temperature of the burned area increased between 1°C and 11°C in comparison to unburned areas (Fig. 6(a) and 6(b)). This situation can be explained by the decrease in albedo, which is the ratio of the reflected radiation to the total radiation. A decrease in albedo increases the radiative energy absorption of the burned forest area, which causes the land surface temperature(s) to rise. To assess the changes in *LST* before and after the fire, a d*LST* map was generated by subtraction (Fig. 6(c)). The correlation between d*LST* and d*NBR* was found to be 0.8, indicating a high correlation (Fig. 6(d)).

Maximum Likelihood classification and support vector machine classification algorithms were applied to the post-fire Landsat 8 satellite image (spectral bands between 2 and 7 with a spatial resolution of 30 m) to map the burned area. The same processes were performed on Sentinel 10 m (spectral bands 2, 3, 4, and 8) and 20 m (all spectral bands). The VISNIR bands of Sentinel data with 10 m spatial resolution were also resampled to 20 m spatial resolution and were used with other original 20 m resolution bands (i.e. 5, 6, 7 and 8a) in the classification. A nearest-neighbor resampling process was applied to evaluate the efficiency of the spatial resolution for classification accuracy. Six training areas were selected on both satellite images, which were burned forest area, lake, bare soil, forest, agriculture, and mining area. Burned forest areas mapped by the ML classification were found to be 962.37 ha, 963.36 ha, and 911.34 ha for 10 m Sentinel, 20 m Sentinel, and 30 m Landsat 8 satellite images respectively. Burned forest areas mapped by the SVM classification were found to be 991.35 ha, 994.65 ha, and 997.11 ha for 10 m Sentinel, 20 m Sentinel, and 30 m Landsat 8 satellite images respectively. The efficiencies of Sentinel 2A and Landsat 8 satellites were compared in terms of overall accuracies after the supervised classification process (Table 8). After comparing the exact burned forest area (986 ha) (obtained

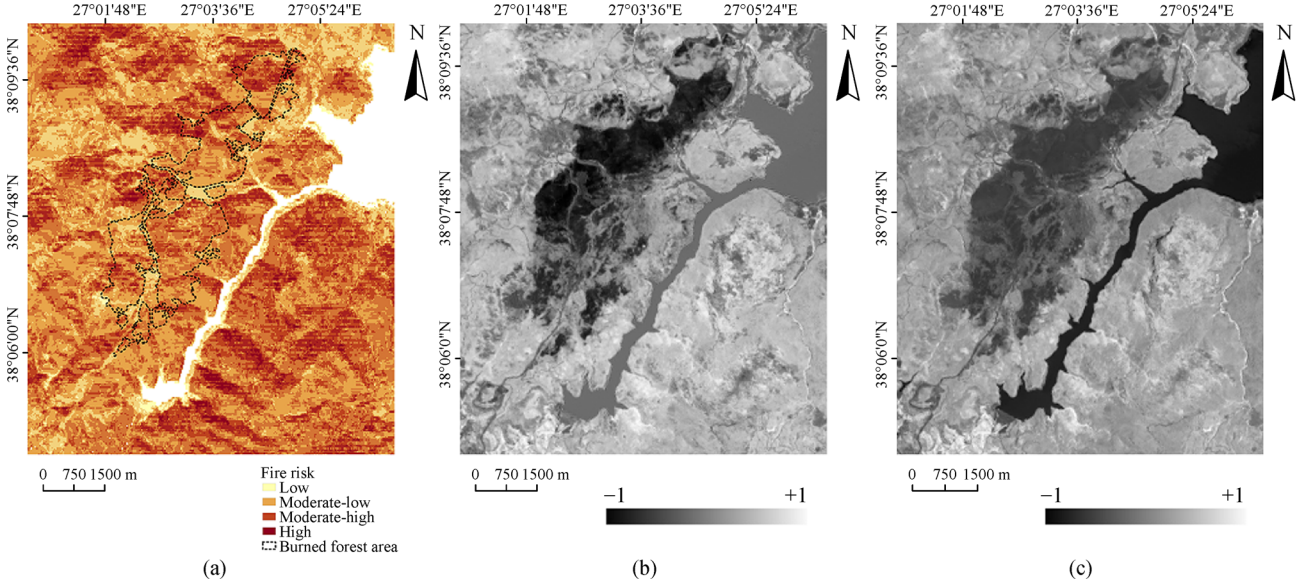

Fig. 4 Fire risk map (a) and Spectral indices (b) *NBR*, (c) *NDVI*.

Table 7 Quantitative analysis of the fire risk in the burned area

	Fire Risk/ha				
Rank	Low	Moderate Low	Moderate High	High	Total
Area/ha	38	329	556	63	986

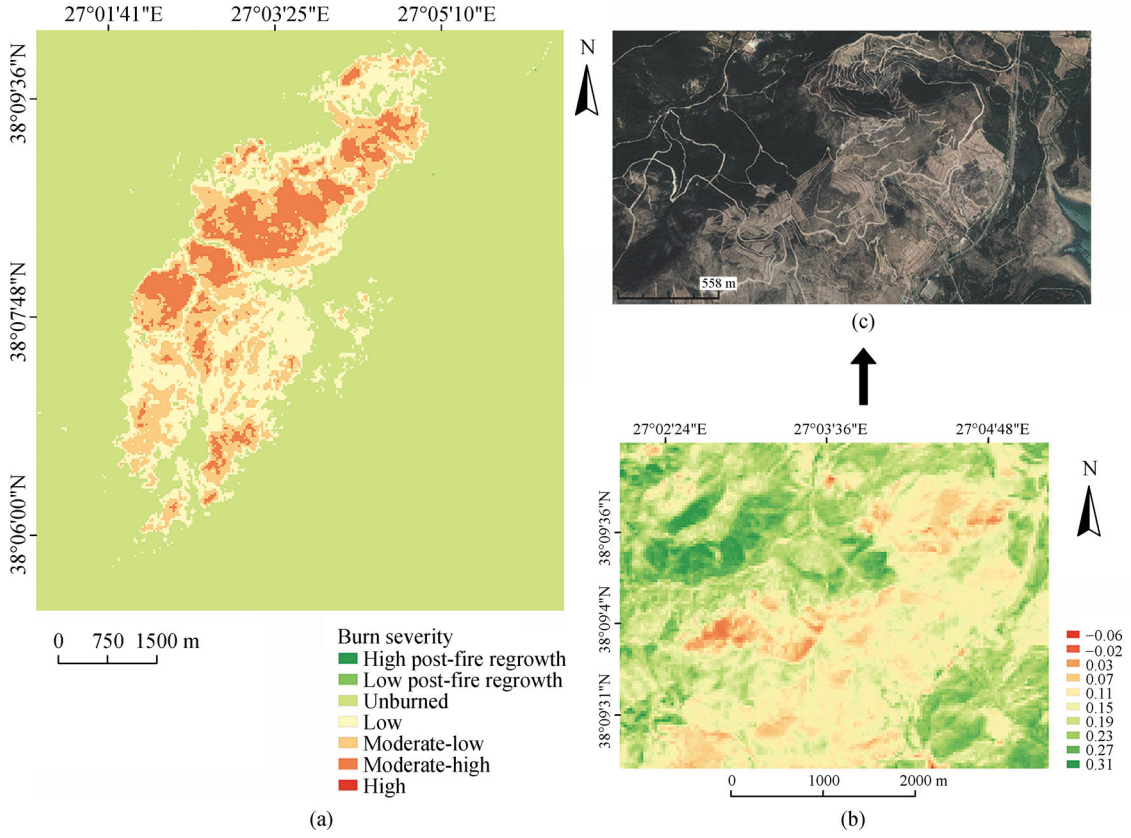

Fig. 5 Burn severity map (a) short-term vegetation survival monitoring, (b) *NDVI* map (01.11.2018), (c) Google Earth view (23.08.2018).

by the Izmir Forestry Chief Directorate) to the thematic classification findings, Sentinel (10 m) image classification was found to give the best results due to its higher spatial resolution (Fig. 7).

To evaluate the relationship between canopy closure, slope and other metrics such as burn severity and *DI*, 1: 25000 scale maps were produced in GIS that showed the canopy closure and slope of the Menderes District (Figs. 8 (a) and 8(b)). The slope map was produced by topographic measurements (produced at 5 m intervals) obtained from field studies carried out by the Izmir Forestry Chief Directorate.

Spatial relationships between slope and canopy closure were separately analyzed in relation to burn severity and disturbance (*DI*). Tables 9 and 10 show that areas with a canopy closure between 71%–100% and a slope above 35% had the highest burn incidence in the region, which confirms that burn severity increases with the rise of both slope and canopy closure. Approximately 80% of the total burned area (986 ha-reference data) had low burn severity, 59% of which had a canopy closure between 71 and 100%, and 1% had less than 11%. Moreover, 57% of the low burn severity area was over the 35% slope range, and 0.1% was in the 0–5% slope range. Furthermore, 5% of the total burned area was found to have a moderate-high burn severity, with 53% within the range of 71%–100% canopy closure. Alternatively, none of the areas with moderate-high burn severity area had less than 11% of canopy closure. 92% of the moderate-high burn severity area had a slope greater than 35%, while no moderate-high burn severity was found in the 0–5% slope range.

Similar to burn severity, the disturbance of the burned area increased with the rise of both slope and canopy closure (Table 10). Results showed that approximately 55% of the total burned area had low disturbance, 73% of which had a canopy closure of 71%–100%. No disturbance was found when canopy closure was less than 11%. Furthermore, 58% of the slope in this area was over 35%, only containing 0.2% of low disturbance area within the 0–5% slope range. Moreover, 1% of the total burned area was found to have high disturbance. 17% of this area was within the range of 71%–100% canopy closure (50% in the range of 41%–71%), while 17% had less than 11%. 83% of the slope in this area was over 35%. No disturbance was recorded in the 0–5% slope range.

Only data from the northern section of the study area was available for use in the spatial distribution analyses of the FRP (MODIS/VIIRS) data and GIS maps. For the confidence level, which gauges the quality of individual hotspot/fire pixels, the nominal-confidence (75% confidence) and high-confidence (100% confidence) *FRP* data were utilized among all available *FRP* data. Figures 9(a) and 9(b) show the spatial distribution of *FRP* data on the slope and burn severity (d*NBR*) maps, where *FRP* values

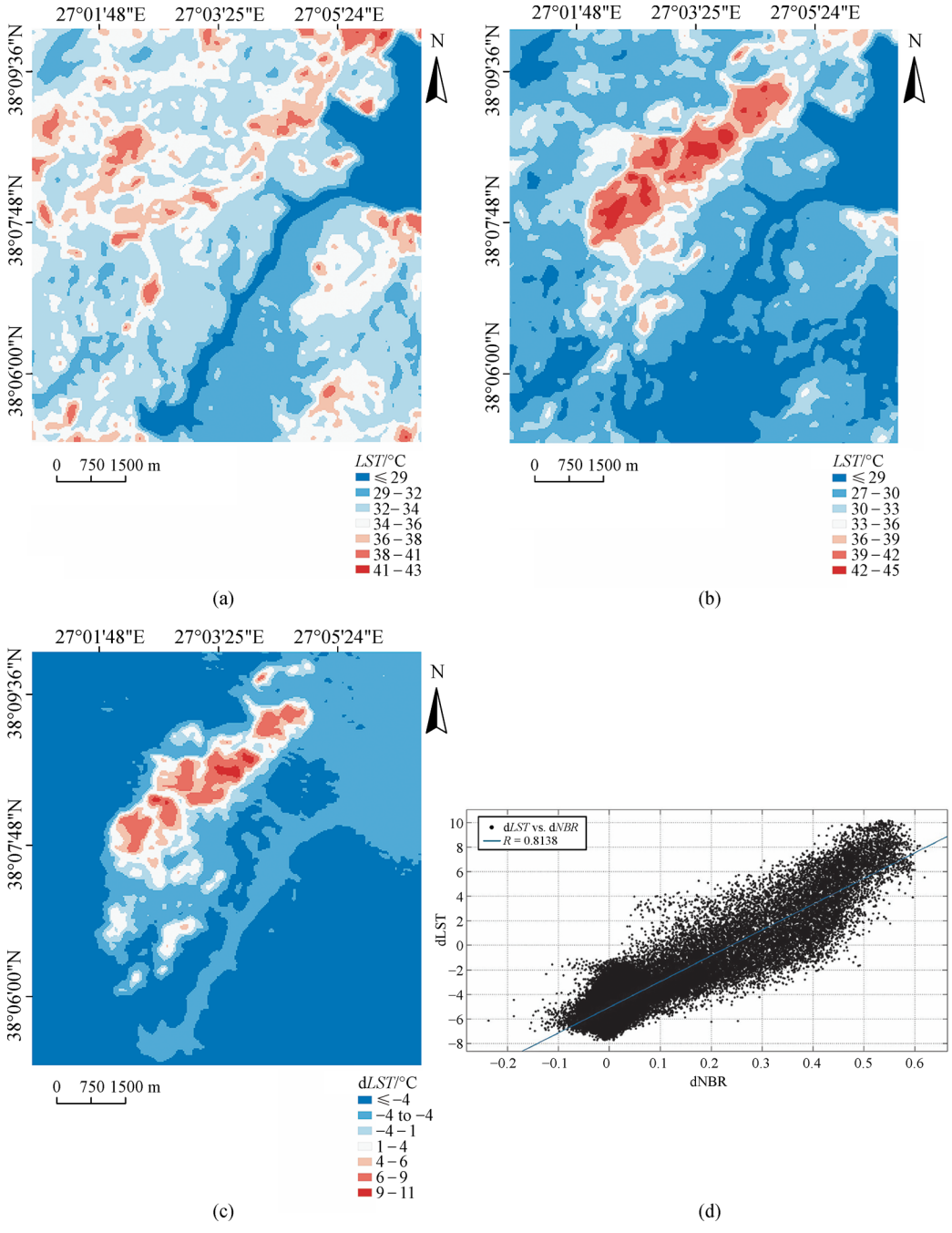

Fig. 6 *LST* maps of burned area produced from Landsat images dated (a) 30.06.2017 and (b) 16.07.2017, (c) d*LST* map, (d) Correlation between d*LST* and d*NBR*.

Table 8 Accuracy assessment of ML and SVM classification results (Appendix A)

Satellite	Maximum Likelihood		Support Vector Machine	
	Overall Accuracy/%	Kappa Coefficient	Overall Accuracy/%	Kappa Coefficient
Sentinel 2 (10 m)	96.43	0.96	99.56	0.99
Sentinel 2 (20 m)	82.22	0.81	97.86	0.97
Landsat 8 (30 m)	80.30	0.79	97.52	0.96

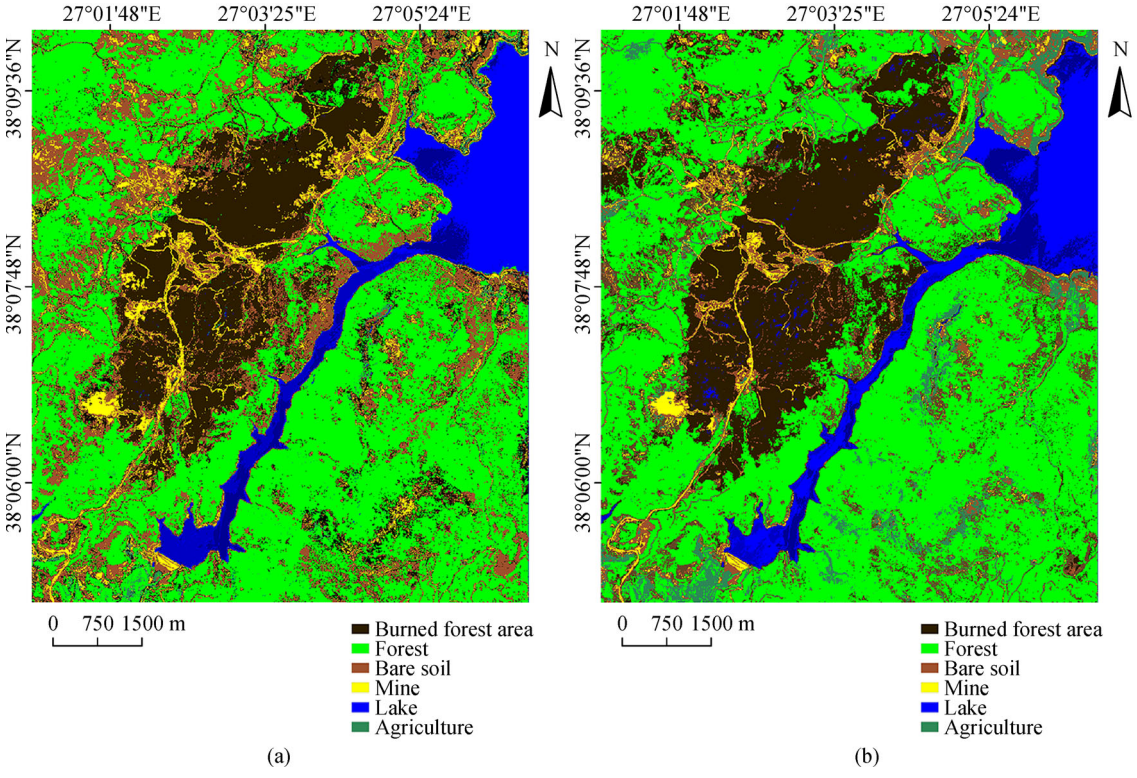

Fig. 7 Sentinel 2 (10 m) post-fire thematic maps. (a) Maximum likelihood, (b) support vector machine.

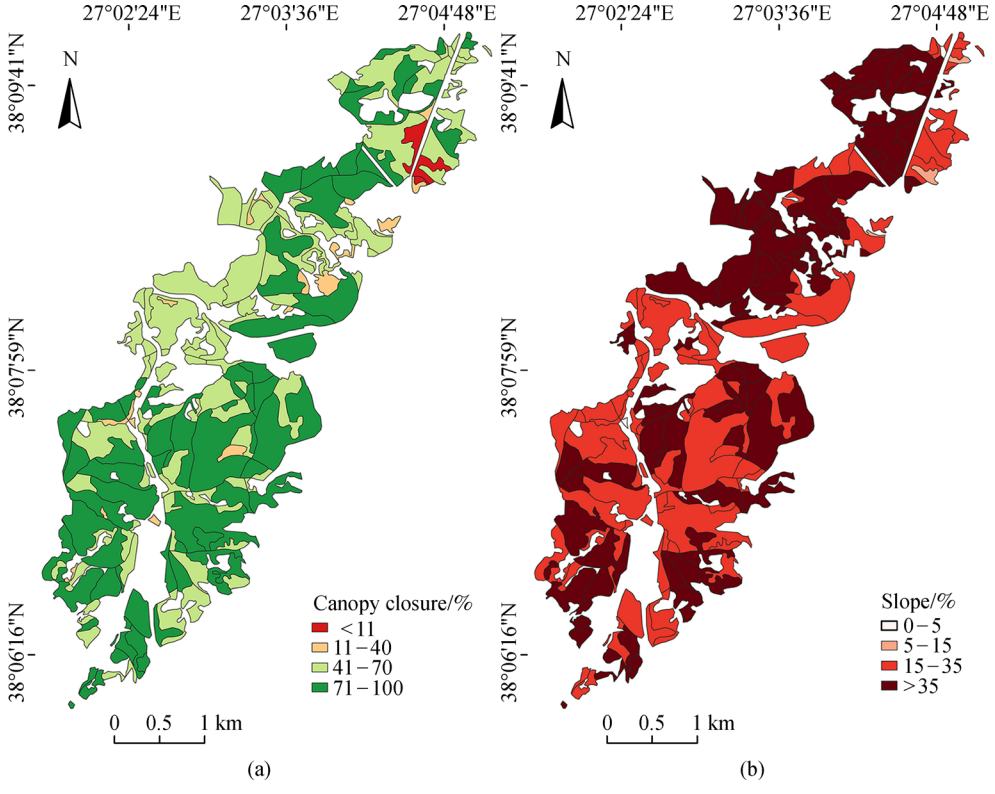

Fig. 8 GIS maps of Menderes region. (a) Canopy closure, (b) slope.

Table 9 The spatial pattern analysis of canopy closure and slope with burn severity

Burn severity /ha	Canopy Closure /%				Total area /ha	Slope /%				Total area /ha
	< 11	11–40	41–70	71–100		0–5	5–15	15–35	> 35	
Low	6	18	298	468	790	1	4	337	448	790
Moderate low	6	7	80	50	143	1	1	54	87	143
Moderate high	0	1	24	28	53	0	0	4	49	53
Σ /ha	12	26	402	546	**986**	2	5	395	584	**986**

Table 10 The spatial pattern analysis of canopy closure and slope with disturbance (*DI*)

Burn severity /ha	Canopy Closure /%				Total area /ha	Slope /%				Total area /ha
	< 11	11–40	41–70	71–100		0–5	5–15	15–35	> 35	
Low	0	2	143	396	541	1	0	225	315	541
Moderate low	0	10	169	124	303	0	5	118	180	303
Moderate high	12	6	67	51	136	0	69	63	4	136
High	1	1	3	1	6	0	0	1	5	6
Σ (ha)	13	19	382	572	**986**	1	74	407	504	**986**

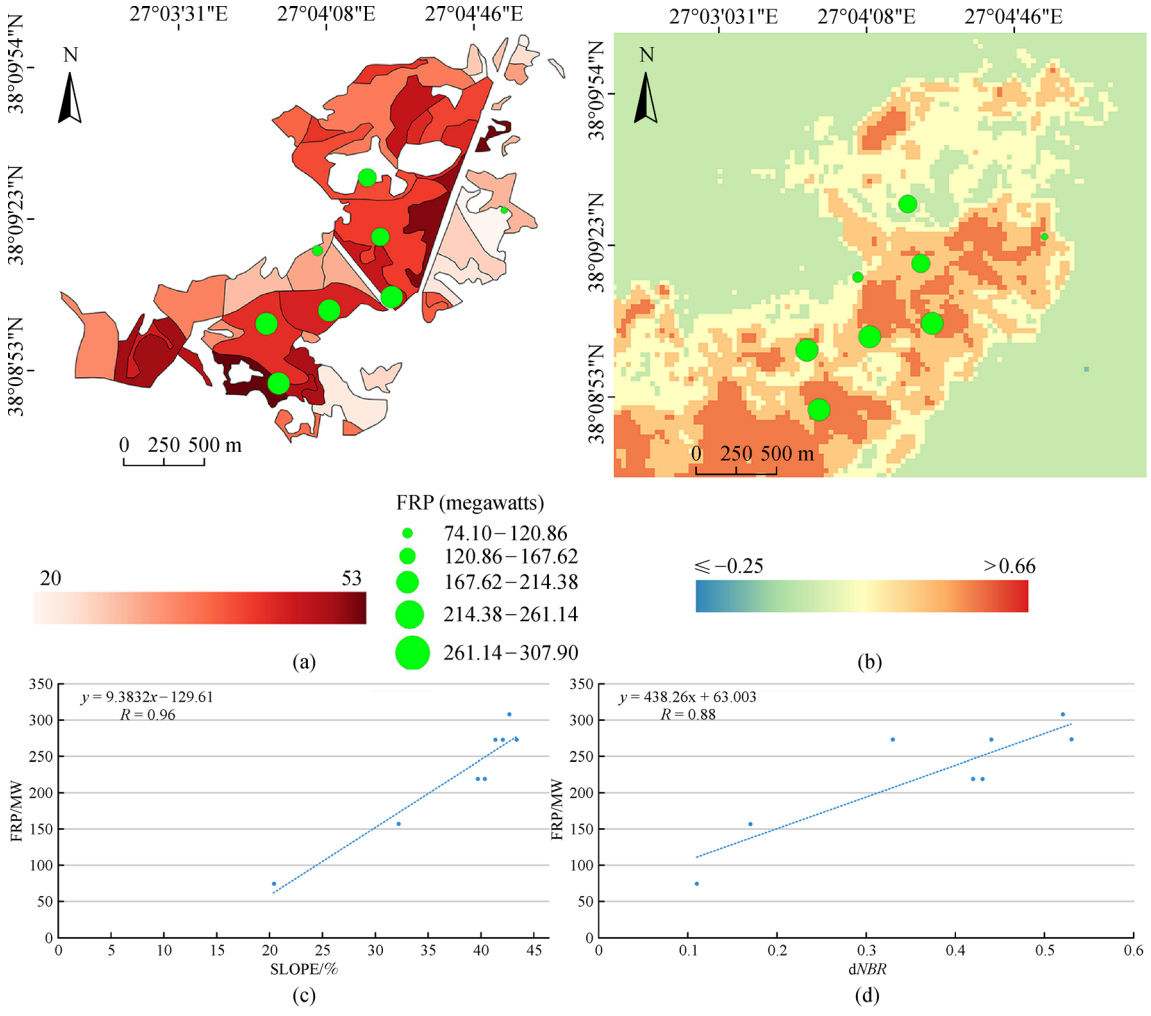

Fig. 9 The FRP data distribution on the (a) slope map, (b) dNBR map. Correlation analysis between (c) FRP-slope, (d) FRP-dNBR.

increase with the increase in slope and burn severity. As expected, *FRP* was found to be highly correlated with both parameters.

Moreover, a correlation analysis between *FRP*-slope and *FRP*-d*NBR* was also performed. As a result, the correlation between *FRP* and slope and *FRP* and d*NBR* was found as 0.96 and 0.88, respectively (Figs. 9(c) and 9(d)).

5 Conclusions

In this study, the forest fire that occurred in Menderes, Izmir was analyzed using pre- and post-fire satellite images, MODIS and VIIRS *FRP* data, and ancillary data (i.e., field data, forest management plans produced by Izmir Forestry Chief Directorate, meteorological data). Fundamental spatial parameters affecting the forest fire were evaluated in GIS.

The *NBR* index was found to be the most successful in distinguishing the burned forest area from healthy forest, and mine and settlement areas. Burn severity was determined from a Landsat 8 satellite image dated July 16, 2017. Post-*NDVI* analysis showed no vegetation growth in the region in the short term after the fire. In parallel, high-resolution satellite imagery (i.e., Google Earth image) revealed the recent mining operation that started in the northern part of the region.

The *LST* maps showed that the temperature of the burned forest area increased from 1°C to 11°C compared to unburned areas as a result of lower albedo. A high correlation ($R = 0.81$) was observed between d*NBR* and d*LST*, indicating that high *LST* corresponded to high burn severity and low *LST* corresponded to low burn severity. According to the supervised classification results, the Sentinel (10 m) image classification gave the best results (96.43% for Maximum Likelihood and 99.56% for Support Vector Machine) due to the higher spatial resolution of Sentinel-2, which leads to a more precise pixel-based mapping of the forest fire disturbance and has two spectral bands — the Red edge band and the narrow NIR band — that heighten the accuracy of the classified image.

This study demonstrates that an integrated approach to remote sensing and GIS can reveal the spatial distributions and correlations between a variety of parameters (slope, canopy closure, *FRP*, etc.) that affect the origin and the spreading of a fire. The results from the spatial pattern analysis in GIS have shown that areas with canopy closure between 71%–100% and slope above 35% had the highest burn incidence. Consequently, burn severity increased with the rise of both slope and canopy closure. Of the total burned area, approximately 80% had a low burn severity and 5% had a moderate-high burn severity, whereas 55% had a low disturbance and 1% had a high disturbance. Moreover, the correlation between *FRP* and slope and *FRP* and d*NBR* was found as 0.96 and 0.88, respectively.

As a result, the integration of remote sensing and GIS techniques was shown to be crucial for assessing the fire damage in the region, such as deforestation, and for monitoring the amount of vegetation regrowth for the sustainability of forest ecosystems. However, recent satellite images on the Google Earth display surface mining operations in the northern section of the region, resulting in the loss of forest habitats. In this context, it is critical that advanced forest fire monitoring systems using geo-information technologies be established to improve the sustainable use of natural forest resources and control negative mining effects.

References

Akkaş M E, Bucak C, Boza Z, Eronat H, Bekereci A, Erkan A, Cebeci C (2006). The investigation of the great wild fires based on meteorological data. Ege Forestry Res I T, 36 (in Turkish)

Boschetti L, Roy D P (2009). Strategies for the fusion of satellite fire radiative power with burned area data for fire radiative energy derivation. J Geophys Res, 114(D20)

Chaparro D, Vall-llossera M, Piles M, Camps A, Rüdiger C, Riera-Tatche R (2016). Predicting the extent of wildfires using remotely sensed soil moisture and temperature trends. IEEE J Sel Top Appl Earth Obs Remote Sens, 9(6): 2818–2829

Chen W, Cao C, Koyama L (2012). Detection of forest disturbance in the Greater Hinggan Mountain of China based on Landsat time-series data. In: 2012 IEEE International Geoscience and Remote Sensing Symposium (IGARSS)

Chowdhury E H, Hassan Q K (2015). Operational perspective of remote sensing-based forest fire danger forecasting systems. ISPRS J Photogramm Remote Sens, 104: 224–236

Chuvieco E, Congalton R G (1989). Application of remote sensing and geographic information systems to forest fire hazard mapping. Remote Sens Environ, 29(2): 147–159

Dağlıyar A, Avdan U, Uça Avcı Z D (2015). Determination of land surface temperature of Kahramanmaras and its environment with the help of remote sensing data. In: TUFUAB VIII. Technical Symposium, Konya (in Turkish)

Díaz-Delgado R, Lloret F, Pons X (2004). Spatial patterns of fire occurrence in Catalonia. Landsc Ecol, 19(7): 731–745

Flannigan M D, Stocks B J, Wotton B M (2000). Climate change and forest fires. Sci Total Environ, 262(3): 221–229

Fraser R H, Li Z, Cihlar J (2000). Hotspot and *NDVI* differencing Synergy (HANDS): a new technique for burned area mapping over boreal forest. Remote Sens Environ, 74(3): 362–376

Gençay G, Birben Ü (2018). Legal process of the mining permits and rehabilitation in the state forests in Turkey—a case of Bartın Forest enterprise. Anatolian Journal of Forest Research, 4(1): 11–12

Giannini M B, Belfiore O R, Parente C, Santamaria R (2015). Land surface temperature from Landsat 5 TM images: comparison of different methods using airborne thermal data. J Eng Sci Technol Re, 8(3): 83–90

Giglio L, Schroeder W, Hall J V, Justice C O (2018). MODIS Collection 6 Active Fire Product User's Guide Revision B

Gonçalves A C, Sousa A M O (2017). The fire in the Mediterranean region: a case study of forest fires in Portugal. Mediterranean Identi: 305–335

Heward H, Smith A M S, Roy D P, Tinkham W T, Hoffman C M, Morgan P, Lannom K O (2013). Is burn severity related to fire intensity? Observations from landscape scale remote sensing. Int J Wildland Fire, 22(7): 910–918

Holden Z A, Smith A M S, Morgan P, Rollins M G, Gessler P E (2005). Evaluation of novel thermally enhanced spectral indices for mapping fire perimeters and comparisons with fire atlas data. Int J Remote Sens, 26(21): 4801–4808

Jaiswal R K, Mukherjee S, Raju K D, Saxena R (2002). Forest fire risk zone mapping from satellite imagery and GIS. Int J Appl Earth Obs Geoinf, 4(1): 1–10

Jimenez-Munoz J C, Cristobal J, Sobrino J A, Soria G, Ninyerola M, Pons X, Pons X (2009). Revision of the single-channel algorithm for land surface temperature retrieval from landsat thermal-infrared data. IEEE Geosci Remote Sens Lett, 47(1): 339–349

Key C H, Benson N C (2005). Landscape assessment (LA) sampling and analysis methods. In: Lutes D C, Keane R E, Caratti J F, Key C H, Benson N C, Sutherland S, Gangi LJ eds. FIREMON: Fire Effects Monitoring and Inventory System. Ogden: USDA Forest Service, Rocky Mountain Research Station, 1–55

Norton J (2008). The use of remote densing indices to determine wildland burn severity in semiarid sagebrush steppe rangelands ssing Landsat ETM + and SPOT 5. Dissertation for Doctoral Degree, Pocatello: Idaho State University

Richards J A (2013). Supervised classification techniques. In: Remote Sensing Digital Image Analysis. Berlin: Springer

Peterson D L, Liittell J S (2013). Risk assessment for wildfire in the western United States. In: VVose J M, Peterson D L, Patel-Weynand, eds. Effects of Climatic Variability and Change on Forest Ecosystems: A Comprehensive Science Synthesis for the U.S. Forest Sector

Platt W J, Orzell S L, Slocum M G (2015). Seasonality of fire weather strongly influences fire regimes in South Florida savanna-grassland landscapes. PLoS One, 10(1): e0116952

Schepers L, Haest B, Veraverbeke S, Spanhove T, Borre J V, Goossens R (2014). Burned area detection and burn severity assessment of a heathland fire in Belgium using airborne imaging spectroscopy (apex). Remote Sens, 6(3): 1803–1826

Seidl R, Thom D, Kautz M, Martin-Benito D, Peltoniemi M, Vacchiano G, Wild J, Ascoli D, Petr M, Honkaniemi J, Lexer M J, Trotsiuk V, Mairota P, Svoboda M, Fabrika M, Nagel T A, Reyer C P O (2017). Forest disturbances under climate change. Nat Clim Chang, 7(6): 395–402

Sivrikaya F, Sağlam B, Akay A E, Bozali N (2014). Evaluation of forest fire risk with GIS. Pol J Environ Stud, 23(1): 187–194

Sonti S H (2015). Application of Geographic Information System (GIS) in forest management. J Geogr Nat Disaster, 5(3): 2167–0587

Sunar F, Özkan Ç (2001). Forest fire analysis with remote sensing data. Int J Remote Sens, 22(12): 2265–2277

Tucker C J (1979). Red and photographic infrared linear combinations for monitoring vegetation. Remote Sens Environ, 8(2): 127–150

US Geological Survey (2016). Landsat 8 (L8) Data Users Handbook, 2016

Vadrevu K, Lasko K (2018). Intercomparison of MODIS AQUA and VIIRS I-Band fires and emissions in an agricultural landscape-implications for air pollution research. Remote Sens (Basel), 10(7): 978

Valero M M, Rios O, Mata C, Pastor E, Plannas E (2018). GIS-based integration of spatial and remote sensing data for wildfire monitoring. In: Earth Resources and Environmental Remote Sensing/GIS Applications IX, Vol. 10790, 107900R

Vlassova L, Pérez-Cabello F, Mimbrero M, Llovería R, García-Martín A (2014). Analysis of the relationship between land surface temperature and wildfire severity in a series of landsat images. Remote Sens, 6(7): 6136–6162

Yu X, Guo X, Wu Z (2014). Land surface temperature retrieval from Landsat 8 TIRS comparison between radiative transfer equation-based method, split window algorithm and single channel method. Remote Sens, 6(10): 9829–9852

Appendix A

Confusion Matrices

SVM–SENTINEL–10 m:

		Truth						
		Burned forest area	Forest	Bare soil	Mine	Lake	Agriculture	Total
Predicted	Burned forest area	49	0	1	0	0	0	50
	Forest	0	50	0	0	0	0	50
	Bare soil	1	0	49	0	0	0	50
	Mine	0	0	0	50	0	0	50
	Lake	0	0	0	0	50	0	50
	Agriculture	0	0	0	0	0	50	50
	Total	50	50	50	50	50	50	300

SVM–SENTINEL–20 m:

		Truth						
		Burned forest area	Forest	Bare soil	Mine	Lake	Agriculture	Total
Predicted	Burned forest area	49	0	1	0	0	0	50
	Forest	0	50	0	0	0	2	52
	Bare soil	1	0	49	0	0	1	51
	Mine	0	0	2	48	0	0	50
	Lake	1	0	0	0	48	0	49
	Agriculture	0	1	0	0	0	47	48
	Total	51	51	52	48	48	50	300

SVM–LANDSAT–30 m:

		Truth						
		Burned forest area	Forest	Bare soil	Mine	Lake	Agriculture	Total
Predicted	Burned forest area	49	0	1	0	0	0	50
	Forest	0	49	0	0	0	3	52
	Bare soil	1	0	49	0	0	1	51
	Mine	0	0	2	48	0	0	50
	Lake	0	0	0	0	49	0	49
	Agriculture	0	1	0	0	0	47	48
	Total	50	50	52	48	49	51	300

ML–SENTINEL–10 m:

		Truth						
		Burned forest area	Forest	Bare soil	Mine	Lake	Agriculture	Total
Predicted	Burned forest area	48	0	0	0	0	0	48
	Forest	0	49	0	0	0	3	52
	Bare soil	3	0	50	0	0	0	53
	Mine	0	0	2	47	0	0	49
	Lake	0	0	0	0	50	0	50
	Agriculture	0	2	0	0	0	46	48
	Total	51	51	52	47	50	49	300

ML–SENTINEL–20 m:

		Truth						
		Burned forest area	Forest	Bare soil	Mine	Lake	Agriculture	Total
Predicted	Burned forest area	41	4	0	0	5	0	50
	Forest	0	41	0	0	4	5	50
	Bare soil	5	0	41	5	0	0	51
	Mine	3	0	5	42	0	0	50
	Lake	0	0	2	1	42	5	50
	Agriculture	1	5	1	0	0	42	49
	Total	50	50	49	48	51	52	300

ML–LANDSAT–30 m:

		Truth						
		Burned forest area	Forest	Bare soil	Mine	Lake	Agriculture	Total
Predicted	Burned forest area	40	0	6	0	0	0	46
	Forest	0	41	0	0	3	5	49
	Bare soil	5	0	40	5	0	0	50
	Mine	0	7	5	40	0	0	52
	Lake	1	6	0	0	41	6	54
	Agriculture	0	5	0	0	4	40	49
	Total	46	59	51	45	48	51	300